Effects of seismogenic width and low-velocity zones on estimating slip-weakening distance from near-fault ground deformation

Xiang Chen [iD] and Hongfeng Yang [iD]

Earth System Science Programme, Faculty of Science, The Chinese University of Hong Kong, Sha Tin, Hong Kong, China. E-mail: hyang@cuhk.edu.hk

SUMMARY
Fault weakening process controls earthquake rupture propagation and is of great significance to impact the final earthquake size and seismic hazard. Critical slip-weakening distance (D_c) is one of the key parameters, which however is of difficult endeavours to be determined on natural faults, mainly due to its strong trade-off with the fault strength drop. An estimation method of D_c proposed by Fukuyama *et al.* provides a simple and direct reference of D_c on real faults from the near-fault ground displacement at the peak of ground velocity (D_c''). However, multiple factors may affect the observed near-fault ground velocity and thus need to be considered when estimating D_c. In this work we conduct 3-D finite element numerical simulations to examine the effects of finite seismogenic width and near-fault low velocity zones (LVZs) on the results of D_c''. In uniform models with constant prescribed D_c, the derived D_c'' values increase with seismogenic width. Furthermore, the scaling between D_c'' and final slip in models with a constant D_c indicates that the scale-dependent feature of D_c'' might not be related to variation in friction properties. With a near-fault LVZ, D_c'' values show significant magnification. The width of the LVZ plays a more important role in enlarging D_c estimation compared to the depth of the LVZ. Complex wavefields and multiple wiggles introduced by the LVZ could lead to delay pick and then cause large deviation. The value of D_c on the fault may be overestimated through D_c'' from limited stations only.

Key words: Friction; Numerical modelling; Computational seismology; Earthquake dynamics; Dynamics and mechanics of faulting.

1 INTRODUCTION

Earthquakes occur when fast slip develops on faults, which has been widely attributed to fault strength weakening. The significant strength reduction with fault slip and slip rate growth was revealed by both laboratory experiments and seismological observations (Wibberley & Shimamoto 2005; Di Toro *et al.* 2011; Goldsby & Tullis 2011; Houston 2015; Viesca & Garagash 2015). Multiple mechanisms have been proposed to cause the coseismic strength weakening, such as thermal pressurization, powder lubrication, flash heating and so on (Reches & Lockner 2010; Goldsby & Tullis 2011; Viesca & Garagash 2015). To depict the strength decline process, a linear slip-weakening law was introduced (Ida 1972) and has been pervasively used in physics-based earthquake simulations (Andrews 1976; Olsen *et al.* 1997; Dunham & Archuleta 2004; Ma *et al.* 2008; Yang *et al.* 2013; Weng *et al.* 2016; Weng & Yang 2018), in which the fault strength drops linearly from static friction to dynamic friction during a portion of slip, known as slip-weakening distance D_c. Tremendous efforts have been made to unravel the riddles of fault weakening process. However, determining the value of slip-weakening distance D_c on natural faults is still a difficult endeavour.

Various attempts have been made and provide basic constraints on D_c and other dynamic source parameters (Bouchon 1997; Ide & Takeo 1997; Nielsen & Olsen 2000; Dalguer *et al.* 2002; Fukuyama 2003; Mikumo *et al.* 2003; Tinti *et al.* 2005a, 2005b; Ma *et al.* 2008; Weng & Yang 2018; Yao & Yang 2020). Kinematic source inversions place well constraints on slip distribution during earthquakes. Slip history on each grid of the fault plane is then derived to determine stress evolution so as to estimate the D_c from the slip-stress history. Such approach was first applied to the 1995 Kobe earthquake from which a depth-dependent D_c distribution was claimed (Ide & Takeo 1997). More earthquakes were investigated by this approach (Bouchon 1997; Tinti *et al.* 2005b). However, kinematic inversion estimation may be limited by resolution and thus biased by factors such as the adoption of source time function and limited bandwidth (Spudich 2005). In comparison, dynamic rupture simulations solve the stress history spontaneously and do not depend on the slip-stress results from kinematic inversions. However, how to obtain reasonable initial conditions is challenging and strong trade-off between slip-weakening distance and the strength reduction exists (Guatteri 2000; Goto & Sawada 2010). Recently, the non-uniqueness in dynamic source parameters could be diminished by using multiple near-field observations (Weng & Yang 2018; Yang & Yao 2019).

An estimation method of D_c value proposed by Fukuyama and Mikumo provides a simple and direct reference of slip-weakening distance on real faults (Fukuyama 2003; Mikumo *et al.* 2003; Fukuyama & Mikumo 2007), based on the proximity between the traction breakdown time and peak slip rate time in the condition of relatively smooth rupture development. When the rupture propagates smoothly, D_c on the ruptured fault, could be approximated by observations at surface stations on the fault at the time of the maximum slip rate (D_c', Fukuyama 2003; Mikumo *et al.* 2003). For off-fault stations, twice of fault-parallel displacement at the time of peak ground velocity, D_c'', was defined as an approximation of the D_c in strike-slip faults (Fukuyama & Mikumo 2007). Therefore, observations at near-fault seismic and geodetic instruments enable a fast estimation of the slip-weakening parameter.

However, near-fault coseismic observations are affected by several factors such as low-velocity fault damage zones (Ben-Zion & Sammis 2003) and seismogenic width (Weng & Yang 2017). Damage zones are pervasively distributed along crustal faults and are characterized by low seismic velocity (velocity reduction around 20–50 per cent), usually with a width of hundreds to thousands metres (Yang & Zhu 2010; Yang *et al.* 2011, 2014, 2020; Yang 2015). The existence of damage zones could not only promote the earthquake ground motion amplitude (Ben-Zion & Aki 1990; Wu *et al.* 2009; Kurzon *et al.* 2014; Yang 2015), but also impact earthquake rupture development (Huang & Ampuero 2011; Weng *et al.* 2016). Since the D_c'' method relies on near-fault observation, the near-fault damage zone, also called the low-velocity zone (LVZ), could affect the estimation of D_c.

Moreover, recent studies obtaining slip-weakening distance from D_c'' method suggest the scale-dependence of D_c'' with earthquake final slip (Fukuyama & Suzuki 2016; Kaneko *et al.* 2017). While according to recent numerical studies, even without the differences in weakening parameters and stress distribution, only variation in seismogenic width would lead to change in the earthquake moment (Weng & Yang 2017). Furthermore, the final earthquake moment may be subjected to hypocentral location and heterogeneous stress distribution although the D_c is uniform on the fault (Yang *et al.* 2019). In order to examine the foregoing factors and effects on D_c estimation, we conduct numerical simulations to investigate the above questions, for a better understanding of near-fault ground deformation and how the estimation of D_c may be affected.

2 MODEL AND METHOD

In this study, we use finite element code PyLith (Aagaard *et al.* 2013) to run 3-D dynamic rupture simulations. The spontaneous rupture is governed by a linear slip-weakening friction law (Ida 1972) shown in eq. (1):

$$\tau\ (\delta) = \begin{cases} \tau_s - \frac{(\tau_s - \tau_d)\delta}{D_c} & \delta \leq D_c \\ \tau_d & \delta > D_c \end{cases}. \tag{1}$$

τ_s and τ_d denote the static frictional strength and dynamic stress on the fault plane, respectively (Table 1). A uniform slip-weakening distance, D_c is set to be 0.4 m, which falls within the range of values that numerical simulations typically select (Day *et al.* 2005; Bizzarri *et al.* 2010; Weng & Yang 2017).

We set a vertical planar strike-slip fault imbedded in a $120 \times 36 \times 30$ km^3 domain, in which all boundaries are absorbing boundaries except the free surface on the top (Fig. 1a). In our models, the ruptures are allowed to propagate to the surface, as the ground velocity of buried-fault rupture may not contain enough

Table 1. Parameters setting in homogenous models.

Fault parameters	Value
Nucleation radius R_{nuc} (km)	4.00
Peak strength, τ_s (MPa)	31.40
Dynamic stress, τ_d (MPa)	27.00
Initial shear stress (nucleation), τ_0^i (MPa)	$0.2 + \tau_s$
Initial shear stress, τ_0 (MPa)	29.00
Slip-weakening distance, D_c (m)	0.40
Poisson's ratio, ν	0.25
Density, ρ (g cm^{-3})	2.705
V_P (km s^{-1})	5.77
V_S (km s^{-1})	3.33
Shear modulus, μ (GPa)	30

information about the slip-weakening distance (Cruz-Atienza *et al.* 2009). The fault plane extends 100 km in along-strike length. We select variant seismogenic widths (w) in depth to investigate their effects.

To initiate the spontaneous rupture, we introduce a circular prestressed nucleation zone in the middle of the seismogenic width, within which the initial shear stress, τ_0^i is slightly higher than the static strength τ_s (Table 1). A proper selection of nucleation zone size should ensure a stable rupture development, shorten the initiation time but also decrease the artificial effect (Bizzarri 2010; Galis *et al.* 2015). The radius of the circular nucleation zone in this study is 4.0 km, which by test could establish stable rupture propagation in the current stress and friction level and also satisfies the estimated critical nucleation threshold (Galis *et al.* 2015):

$$R_{\text{nuc}} = \frac{\pi}{4} \frac{1}{f_{\text{min}}^2} \frac{\tau_s - \tau_d}{(\tau_0 - \tau_d)^2} \mu D_c. \tag{2}$$

R_{nuc} refers to the critical nucleation zone radius of breakaway rupture, and f_{min} is the minimum of the function:

$$f\ (x) = \sqrt{x}\ \left[1 + \frac{\tau_0^i - \tau_0}{\tau_0 - \tau_d}\left(1 - \sqrt{1 - 1/x^2}\right)\right], \tag{3}$$

where τ_0^i is the initial shear stress inside the nucleation zone, and τ_0 is the initial shear stress on other parts of the fault plane. Appling the values in Table 1, $f_{\text{min}} \approx 1.626$ and the critical nucleation size is $R_{\text{nuc}} \approx 3.92$ km. Our selection of nucleation radius $R_{\text{nuc}} = 4.0$ km just meets the requirement of critical nucleation size to ensure a continuous propagation on the entire fault thus we could calculate the D_c'' with smooth rupture propagation.

In the simulations with low-velocity zones, we set a finite low-velocity region confined by L_d in depth and L_w in the faultnormal direction (Fig. 1b). The velocity reductions observed at different faults range from ~20 to 50 per cent (Yang 2015). Here the velocity reduction is set at a fixed value 30 per cent, that is $\frac{V_P - V_{P,L}}{V_P} = \frac{V_S - V_{S,L}}{V_S} = 30$ per cent, in which V_P and V_S represent the P- and S-wave velocities in the surrounding rocks (same as that in homogeneous models, shown in Table 1), while $V_{P,L}$ and $V_{S,L}$ refer to the P- and S-wave velocities in the LVZ, respectively. For simplicity, we set uniform density in the whole model.

Calculating D_c'' demands good spatial and temporal resolution near the passage of rupture tips. To achieve a good spatial resolution in rupture tips and a convergent numerical result requires three or more grids inside the cohesive zone (Day *et al.* 2005). The cohesive zone refers to the area behind the rupture tip where shear stress decreases from peak strength to dynamic friction. An estimation of the static cohesive zone length for linear slip-weakening law is
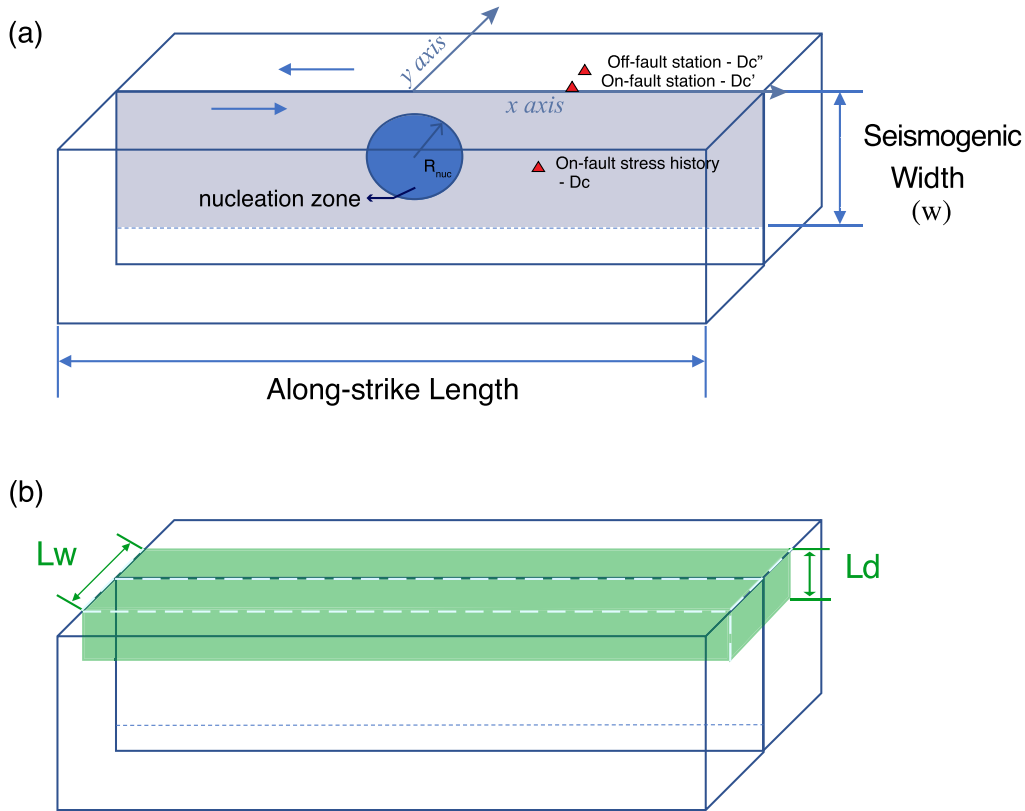
Figure 1. (a) Model setup of rupture simulation. We set a left-lateral strike-slip fault model in this study. The navy circle in the centre shows the nucleation zone location; the light blue band indicates the seismogenic fault zone. The x, y axes correspond to the ground coordinate axes used in the following D_c'' distribution figures. Red triangles represent virtual stations to infer D_c, D_c' and D_c'', respectively. (b) Illustration of the model with a low-velocity zone. The LVZ is shown in light green. L_w refers to the LVZ width in the fault-normal direction; L_d indicates the LVZ depth.

given in eq. (4) (Palmer & Rice 1973; Day *et al.* 2005):

$$\Lambda_0 = \frac{9\pi}{32} \frac{\mu}{1-\nu} \frac{D_c}{\tau_s - \tau_d}. \tag{4}$$

The grid size is $\Delta x = 200$ m in all models. Substituting the material property parameters in Table 1 into eq. (4), for homogeneous models $\Lambda_0/\Delta x \approx 16$, while for the low-velocity zone with 30 per cent velocity reduction $\Lambda_0/\Delta x \approx 7$, both meeting the numerical requirements. We also conduct convergence tests using grid sizes of 150 and 250 m. The slip distribution and slip rate on the fault indicate that the numerical solutions are well converged for the grid sizes of 150 and 200 m (Fig. S1). Comparison of ground velocities from models of different grid sizes also confirms that our choice of 200 m is sufficiently small to resolve the rupture process in our models (Fig. S2). The selection of time interval is $\Delta t = 0.01s$ in this study, which satisfies the Courant–Friedrichs–Lewy law (Courant *et al.* 1928) that the Courant–Friedrichs–Lewy ratio CFL $= V_p \, \Delta t / \Delta x < 0.71$.

3 DATA PROCESSING AND RESULTS

We nucleate ruptures at $x = 0$ and output ground velocities and displacements from each dynamic rupture scenario (Fig. 2a). In the homogeneous model ($w = 15$ km), if we track one point on the fault plane, the traction breakdown time and slip history indicate that D_c is 0.4 m (Fig. 2b), as we defined. For the record at the surface (Fig. 2c), D_c' is measured at the time when slip rate on the fault reaches the peak value (Mikumo *et al.* 2003; Fukuyama

2003). Similarly, a D_c'' value is inferred at a station that is 0.2 km away from the fault at the time when fault-parallel velocity (FP velocity) reaches the maximum (Fig. 2d). By far this method has been applied to a few earthquakes (Table 2). Due to the limited instrument coverage, it is uncommon to have near-fault records that capture the coseismic ground motion. In the existing cases (Table 2), near-fault seismic stations distribute from the ruptured faults with distances of 0.1–3 km. In our numerical simulations, we calculate and analyse D_c'' in one quadrant on the ground surface with off-fault distance up to 3 km, according to the observations.

3.1 Effects of filtering and coherency of ground velocities on estimating D_c''

To obtain consistent and reliable D_c'' values, we need to pre-process the fault-parallel ground velocity data output from model simulations. The peak velocity time directly inferred from the raw data may be affected by the high-frequency spikes in simulated waveforms. For instance, the peak velocity time on the raw data is slightly advanced comparing with that from the lowpass filtered data (Fig. 2d). In addition, the peak value is very close in the next wiggle and thus if we track the peak value in the raw data, we may obtain fluctuated D_c'' distribution (Fig. 3a). As the high-frequency contents in the waveforms appear to depend on the grid size (Fig. S2), they are likely numerical noises and do not represent the accurate synthetic ground velocities. As such, we apply a lowpass filter to remove the high-frequency wiggles in ground velocity data and obtain stable D_c'' values after applying a 2 Hz zero-phase lowpass filter (Fig. 3b).
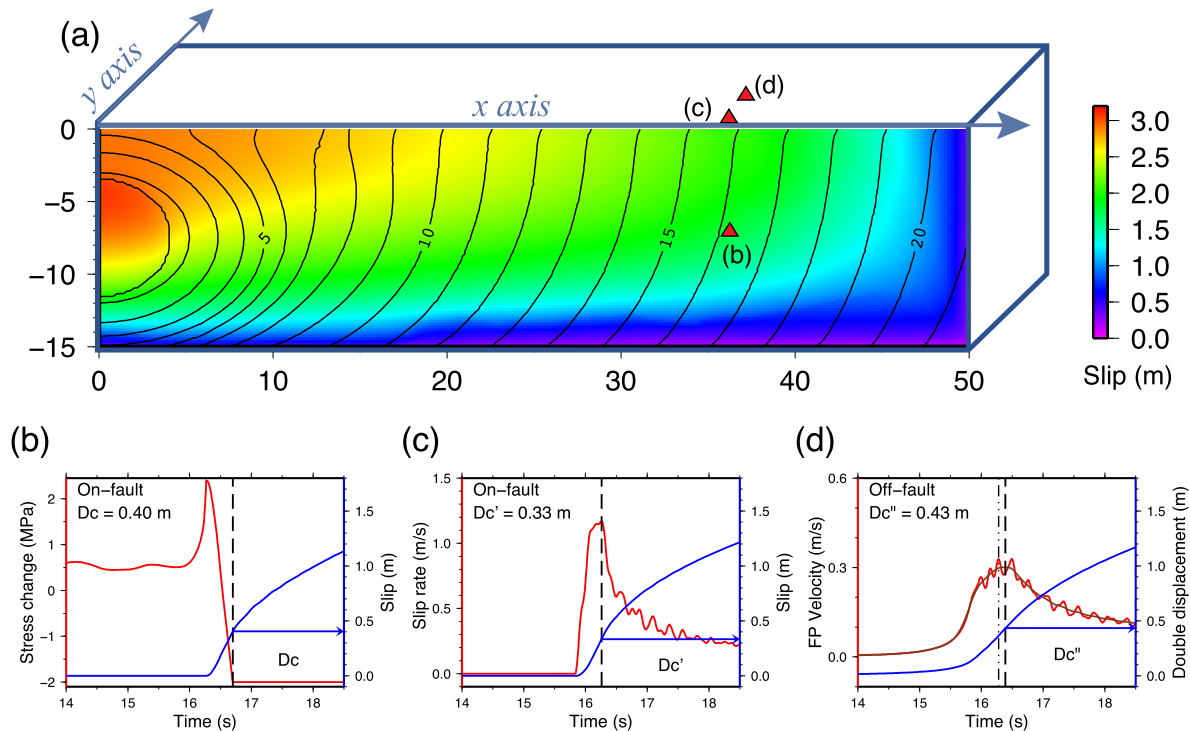
Figure 2. Illustration of determining D_c, D_c' and D_c''. (a) Cutting profile of slip on the fault plane of a uniform model with $w = 15$ km. The contours are isochrones of rupture fronts. Red triangles correspond to the locations to obtain D_c, D_c' and D_c'' in subfigures (b), (c) and (d). (b) Stress (red) and slip (blue) history of the on-fault grid at $x = 36.4$ km, depth $= -7.4$ km. The dashed line indicates the stress breakdown time and the corresponding slip value is D_c. (c) Time history of slip rate (red) and slip (blue) of the on-fault grid at $x = 36.4$ km, depth $= 0$ km. The dashed line indicates the time of the peak slip rate; D_c' is inferred at the corresponding slip value. (d) Time history of fault-parallel velocity (red) and displacement (blue). The amplitude of displacement is doubled for estimation of D_c'' in the strike-slip fault model. The brown curve shows the waveform with a 2 Hz lowpass filter applied. The dashed line and the dashed–dotted line mark the peak velocity time of the filtered waveform and the raw data, respectively. $D_c'' = 0.43$ m is obtained from the filtered data.

**Table 2.** Application cases of D_c'' method.

Earthquake and station info	Magnitude	D_c''	Station off-fault distance	Total slip (*)	D_c''/total slip	Distance from epicentre	References
2000 Tottori	M_w 6.6	0.3 m	0.1 km	1 m	0.3	~4.7 km	(Mikumo *et al.* 2003; Fukuyama & Mikumo 2007)
2002 Denali	M_w 7.9	2.5 m	~3 km	6.5 m	0.38	~85 km	(Fukuyama & Mikumo 2007)
2016 Kumamoto	M_w 7.1	1 m	0.5 km	~2.3 m	0.43	~7 km	(Fukuyama & Suzuki 2016)
2016 Kaikoura	M_w 7.8	4.9 m	2.7 km	14 m	0.35	~115.6 km	(Kaneko *et al.* 2017)

*The slip amounts here refer to local slip values.

Comparing to the D_c'' results obtained from raw data (Fig. 3a), random values with large deviations from the true D_c value are removed (Fig. 3b).

In order to pick stable and continuous time moments automatically, we need to select a reasonable frequency range for the synthetic data. To test the potential bias introduced by the filter, we

check the frequency effects from 0.5 to 3 Hz on ground velocity. For the ground velocity waveform from a homogeneous model ($w = 15$ km), decreasing cut-off frequency would cause slight delay of peak velocity time (Fig. 4a) and thus leads to overestimation of D_c'' with lower cutoff frequency. To remove all the local wiggles but keep the shape of ground velocity pulse as much as possible,
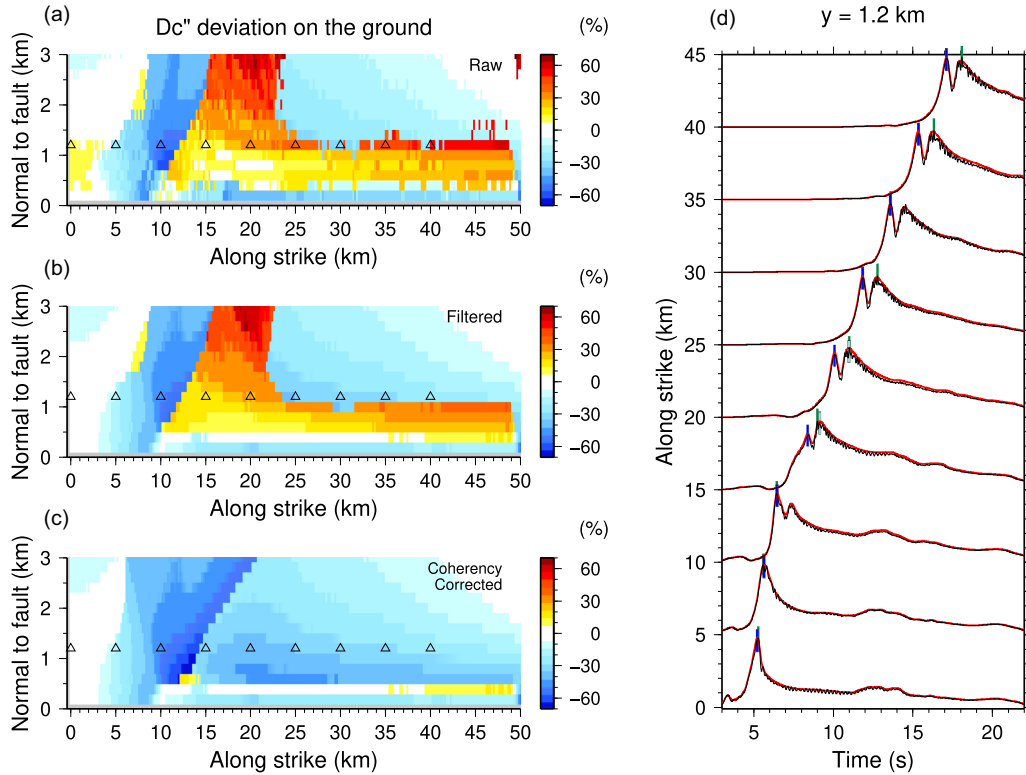
Figure 3. Data processing with filter and coherency correction. (a) D_c'' deviation degree (i.e. $\frac{D_c'' - D_c}{D_c}$, D_c is constant, 0.4 m) inferred from the raw data [corresponding to dark green time ticks in (d)]. Triangles represent the virtual station locations of the profile shown in (d). (b) D_c'' deviation degree with a filter applied. The peak time to infer D_c'' is selected from 2 Hz lowpass filtered velocity waveforms [corresponding to light green time ticks in (d)]. (c) D_c'' deviation degree after coherency correcting [corresponding to blue time ticks in (d)]. (d) Fault-parallel velocity profile along the strike direction [profile location at $y = 1.2$ km, shown as triangles in (a) to (c)]. Red curves are 2 Hz lowpass filtered velocity waveforms, beneath which black curves show the raw data. Blue ticks mark the picked time t_p to determine D_c'' after coherency correcting. Light green ticks show the time of the maximum velocity from the filtered data. Dark green ticks exhibit the time of the maximum velocity from the raw data. For the traces with ticks overlapped, the plotting order of ticks is raw (dark green), filtered (light green) then coherency corrected (blue).

we chose 2 Hz as the cutoff frequency and apply it to all the models. Comparison of D_c'' values with different lowpass filters shows that the D_c'' values become stable for cutoff frequency up to 2 Hz (Figs 4b–d). For most of the grids, D_c'' difference introduced between 2 and 3 Hz filter is less 0.05 m (Fig. 4b).

In addition to the effects of filtering, we find that inconsistent phase picking at off-fault locations may also play a role in estimating the D_c'' values. Previous studies get D_c'' at the time of the maximum fault-parallel ground velocity (Fukuyama & Mikumo 2007; Fukuyama & Suzuki 2016; Kaneko *et al.* 2017). However, our synthetic ground velocity shows that latter phase may exhibit larger amplitude (Fig. 3d, shown as light green ticks on filtered waveforms). When using the maximum velocity to mark the passage of the rupture front, inconsistent phases may be used to mark D_c'' (Fig. 3d). In simulation, we have the advantage to set numerous virtual stations to obtain the D_c'' from the consistent phases; so we track the consistent phases to mark D_c'' from the location above nucleation centre ($x = 0$) and obtain the D_c'' distribution from coherent phases (Figs 3c and d).

To obtain D_c'' values from consistent velocity phases, we use the following criteria to pick the first main peak velocity related with the rupture front. For the ground grids nearest to the fault, the shape of the velocity waveform is a clear single pulse, and we track the maximum velocity as t_p (peak velocity time corresponding to D_c'') from the initial centre along the fault strike. For other ground grids, we search the first local maximum velocity within a 3-s time

window according to the t_p of its most adjacent grid closer to the fault. We take this time moment as the rupture-related peak velocity time, t_p, of the grid so as to mark the corresponding double displacement as D_c''. The purpose of setting a search window is to track the first rupture-related phase and avoid the deviation caused by multiwiggles and potential multirupture phases. Animations of fault slip rate and fault-parallel ground velocity (Supplementary animation SM1) development have been inspected to confirm that our selected first peaks are related to the passage of rupture fronts.

After correcting coherency in phase picking, the D_c'' values appear to be mostly underestimated (Fig. 3c). Before coherency correction, there is a zone with fault-normal distance less than ∼1 km with overestimated values (Figs 3a and b). In addition, such overestimations become severe in a region with fault-normal distance up to 3 km with along-strike distances of ∼10–22 km (Figs 3a and b), corresponding to the initial stage of the rupture that nucleated from $x = 0$. Although such overestimations are removed by picking coherent phases, in the area associated with initial rupture stage the D_c'' values are significantly underestimated (Fig. 3c). Thus we only use the region where the stable rupture is established on the fault in the following statistics. We use the D_c'' values on the ground surface in a 20 km (along-strike) × 3 km (fault-normal) area. The range in along-strike direction is 25–45 km from the nucleation zone. The selection in fault-normal direction of 3 km is based on the largest off-fault distance of the station (3 km, Table 2) used to obtain D_c'', in the 2002 Denali earthquake (Fukuyama & Mikumo 2007).
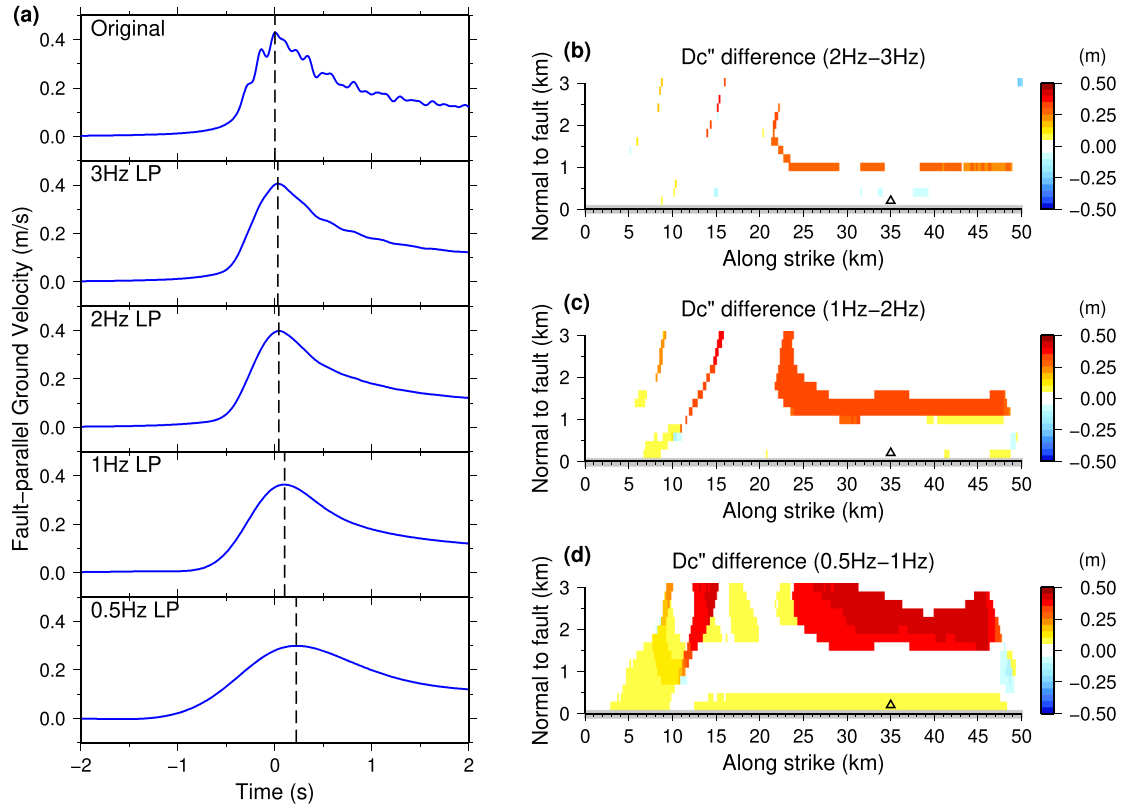
Figure 4. Comparison of different lowpass filter bands. (a) Original ground velocity waveform output from the model and lowpass filtered waveforms with cutoff frequency at 3, 2, 1 and 0.5 Hz, respectively. Waveforms are extracted from the grid at $x = 35$ km, $y = 0.2$ km [shown as triangles in (b)–(d)] of a uniform model with a seismogenic width $w = 15$ km. (b) Differences between D_c'' values with peak time obtained from 2 and 3 Hz lowpass filtered waveforms. (c) and (d) are similar to (b), but the compared lowpass filters are 1 and 2 Hz, and 0.5 and 1 Hz, respectively.

3.2 D_c'' values of homogeneous bounded-seismogenic faults

As investigated by the recent study (Weng & Yang 2017), width of the seismogenic fault may affect the rupture development and the final earthquake scale. So we conduct simulations with variant seismogenic widths to evaluate the effects on D_c'' values. We show the D_c'' distribution of uniform models with seismogenic widths ranging from 10 to 20 km (Fig. 5), which are typical for crustal strike-slip faults. These models with different seismogenic widths have constant $D_c = 0.4$ m and all other parameters as the same (Table 1). The output fault-parallel ground velocities are processed by the above procedure with filtering and coherency correction. The obtained D_c'' on the ground is shown as deviation degree from prescribed D_c (i.e. $\frac{D_c'' - D_c}{D_c}$).

In general, D_c'' increases with seismogenic width (Fig. 5). After coherency correction for models with narrower seismogenic width, especially $w \leq 15$ km, D_c'' underestimates the real D_c for most grids in the selected area. In the model with $w = 10$ km, the largest D_c'' deviation is around 57 per cent from prescribed D_c in the near-fault region of the stable rupture segment. Overestimating appears as seismogenic width gets larger, which mainly occurs in the region further away from the fault trace, especially in the model with $w = 20$ km (Fig. 5e). The large D_c'' values in the zone of ∼2 grids from faults are produced by the waveform change from single pulse to double peaks of fault-parallel velocity. We calculate the average D_c'' in the selected area and find a linear increasing trend (Fig. 6a), although the prescribed D_c on the fault is

a constant. Standard variation of D_c'' ranges from 0.1 to 0.2 m for $D_c = 0.4$ m.

As the D_c'' is determined by the shape and integral of fault-parallel velocity, we compare the velocity waveforms from models with different seismogenic widths on the ground surface. We extract fault-parallel velocity waveforms from the same ground location and align them at the selected peak time t_p (Fig. 6b). Amplitudes of the selected velocity peaks increase significantly with seismogenic width, but the time durations before reaching the peaks are similar (Fig. 6b), which leads to growing integral values at time t_p, that is D_c''. In comparison, the slip rate on the fault shows the similar features as ground velocity, with peak values increasing with seismogenic width while time durations are similar (Fig. 6c).

The deviation from real D_c is explicitly shown on stress reduction history (Fig. 6d), in which peak velocity time (shown as dots in Figs 6c and d) arrives earlier than stress breakdown time. Thus, the deviation occurs with on-fault D_c' (shown in Fig. S3). As seismogenic width decreases, stress reduction rate gets slower, and the advance in time of peak velocity than the stress breakdown time gets larger. This is why the D_c'' underestimation gets more significant at narrower seismogenic width (Fig. 6d). Such difference is predicted by the faster strain energy release rate for models with larger seismogenic widths. According to Day (1982), strain energy released rate at rupture tips could be approximated by

$$G \approx \frac{\pi}{2} \left(\frac{V_S}{V_R} \right)^2 \frac{\mathcal{R}(V_R)}{\sqrt{1 - \frac{V_R^2}{V_S^2}}} \cdot \frac{\Delta \tau^2}{\mu} w \qquad (5)$$
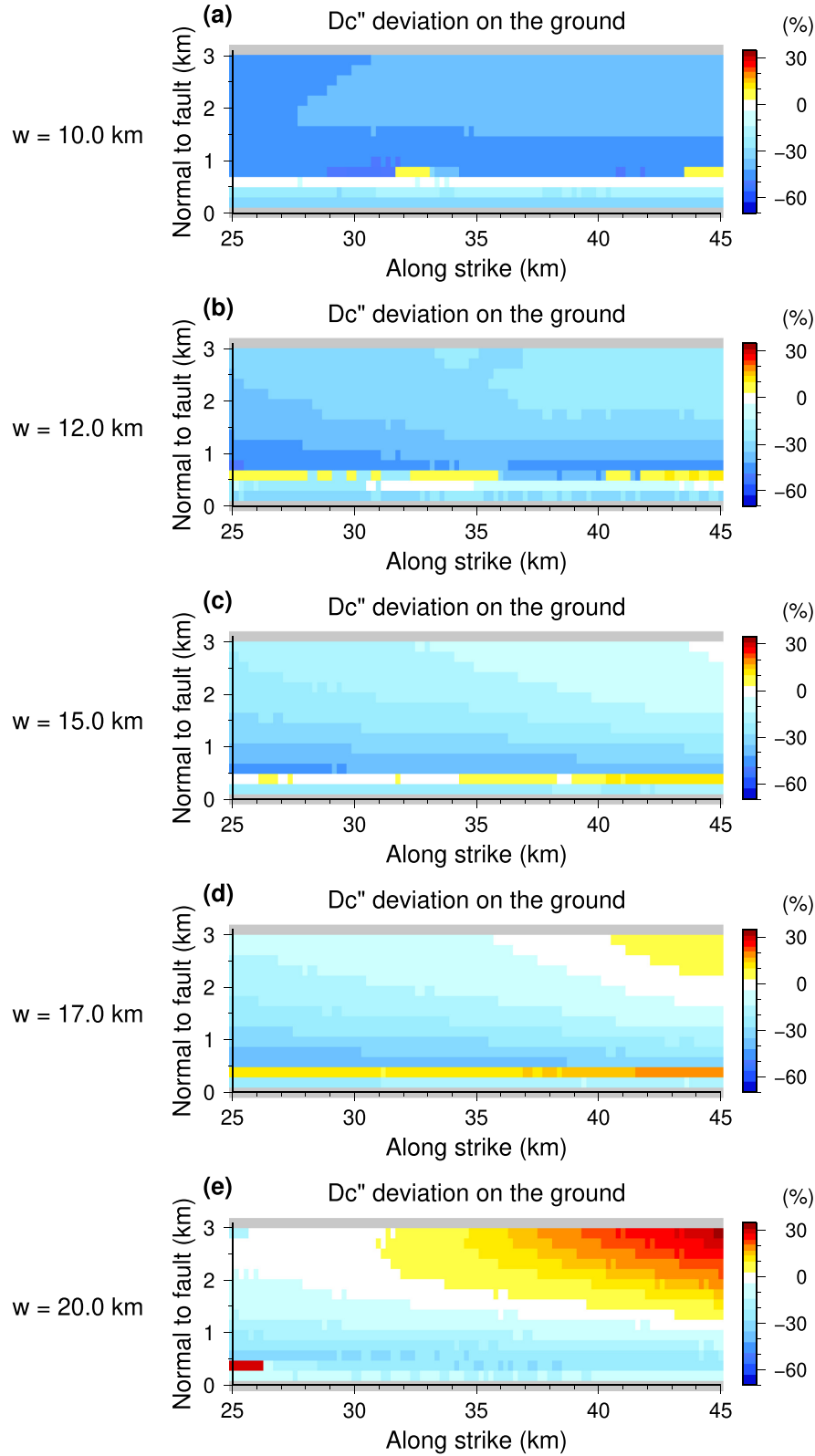
Figure 5. D_c'' deviation degree after filter and coherency correction applied in the selected region. Panels (a)–(e) are of uniform models with seismogenic widths of 10, 12, 15, 17 and 20 km, respectively.

in which V_R is the rupture speed, $\mathcal{R}$ is the Rayleigh function ($\mathcal{R}(c) = [\sqrt{1 - \frac{c^2}{V_P{}^2}}\sqrt{1 - \frac{c^2}{V_S{}^2}} - (1 - \frac{c^2}{2V_S{}^2})^2]$), $\Delta\tau = \tau_0 - \tau_d$, and w is the seismogenic width. Thus, width will impact the stress reduction rate and the deviation between D_c' and D_c.

Along the fault-normal direction, waveforms distort from impulsive forms (with a single peak) to ramp-like forms (with multiple wiggles) as away from the fault surface (Fig. 7a), which is responsible for the coarse D_c'' distribution in that direction (Fig. 7b). In
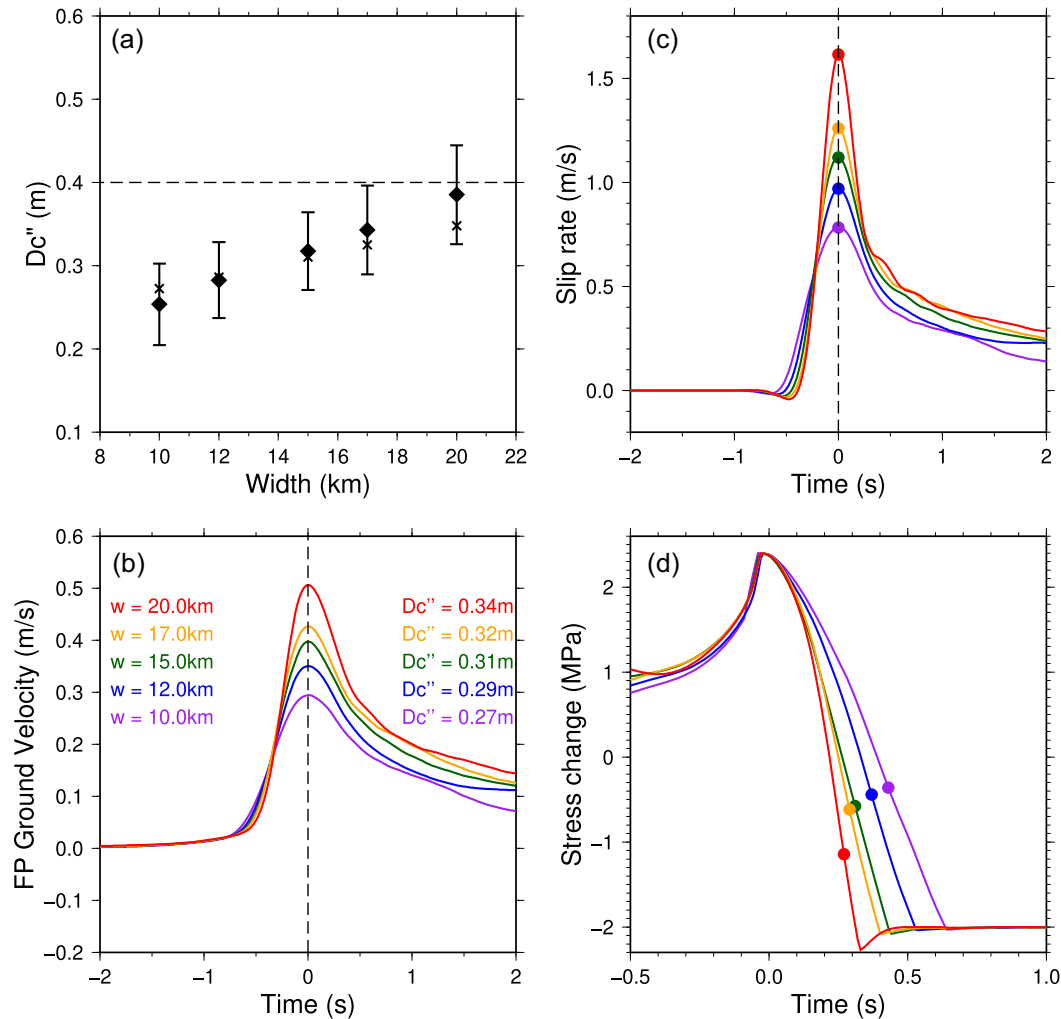
Figure 6. (a) Average D_c'' values versus seismogenic width in uniform models. Diamonds are the average D_c'' values calculated in the selected region shown in Fig. 5. Error bars indicate the standard deviations of D_c''. The crosses show the average D_c'' values of grids with the nearest off-fault distance $y = 0.2$ km. (b) Ground velocity waveforms from models with variant widths aligned at the peak velocity (extracting from the same position: $x = 35$ km, $y = 0.2$ km). (c) Slip rate time series from models with variant widths aligned at the peak slip rate (extracting from: $x = 35$ km, $z = 0$ km). A 2 Hz lowpass filter is applied on waveforms in (b) and (c). (d) Shear stress time evolution aligned at the peak strength. Solid dots denote the time points of peak slip rate as shown in (c). Colour legends of waveforms are shown in (b) corresponding to the widths.

the transition zone of the waveform change, the effects on D_c'' are complicated. For the off-fault grids where the shape change impends ($y = 0.4$ km in Fig. 7b), the latter wiggle grows into undistinguishable with the first pulse and causes a widen velocity pulse and thus delayed peak time t_p, leading to large D_c'' values at t_p. Further away from the fault ($y = 0.6$ km in Fig. 7b), D_c'' decreases quickly once the multiwiggle shape is formed. Then D_c'' increases gradually with fault-normal distance as velocity waveforms get wider (Fig. 7a). The D_c'' variation related to waveform distortion could be around 15–50 per cent in the transition zone (Fig. 8). Except in this region, the D_c'' values at both the nearest and away from fault distances show positive correlation with seismogenic width.

3.3 D_c'' values of models with LVZs

Around the seismogenic fault surface, we set the LVZ (Fig. 1b) to investigate the D_c'' values when there is a near-fault damage zone. In Fig. 9, we show the D_c'' and waveforms on the ground of a LVZ model in which a 2.4-km-wide L_w and 3-km-deep L_d low-velocity

zone with 30 per cent velocity reduction is inserted around the fault plane. With the existence of the low-velocity zone, D_c'' values appear to overestimate the D_c, because ground velocities and displacements are amplified by the LVZ. After filtering and correcting coherency, D_c'' values from the LVZ model (Fig. 9a) could be larger than twice of D_c'' in the homogeneous model (Fig. 3c), especially near the fault trace. Besides, enlargement of D_c'' not only occurs within the LVZ area (Fig. 9a). It affects a broader area beyond the low-velocity range. After the coherency correction, the overestimate could be more than 100 per cent in the near-fault region (Fig. 9a).

Moreover, the LVZ leads to multiple wiggles and more complex wavefields in the near-fault ground velocity (Figs 9c and d). The later seismic phase might have larger amplitude than the first rupture related phase (shown as light green and blue ticks, respectively, in Figs 9c and d), leading to overestimates of real D_c when calculating D_c'' at the maximum velocity time (Fig. 9b). The deviation degree from real D_c could be larger than 200 per cent in near-fault regions if we do not follow the coherent phase (Fig. 9b).
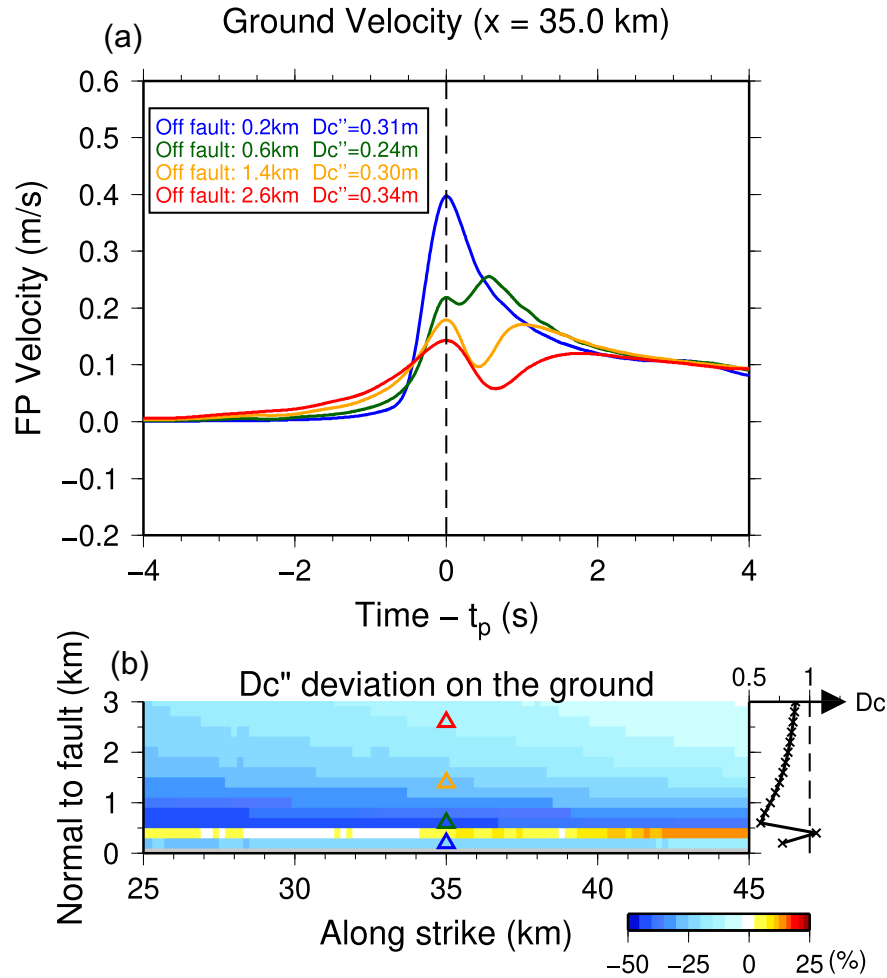
Figure 7. (a) Velocity waveform variation in the fault-normal direction. The fault-parallel velocity waveforms are aligned at the picked time t_p and are from four grids with different fault-normal distances ($x = 35$ km). The off-fault distances and corresponding D_c'' values are shown in the legend. A 2 Hz lowpass filter is applied on waveforms. (b) Ground distributions of D_c'' deviation degree. Triangles represent the locations of the four selected grids in (a). The colours of triangles and waveforms are corresponding to each other. The crosses and the line on the right of (b) show the average D_c'' trend in the fault-normal direction. The unit is the multiple of the real D_c.

Furthermore, the geometric structure of the LVZ varies for different fault systems. To investigate the effects of LVZ geometry, we change the LVZ width (L_w) from 1.2 to 2.4 km, depth (L_d) from 1.0 km to 5.0 km and calculate the average D_c'' of the selected area using the first rupture related phase (Fig. 10a). By changing geometry of the LVZ, we find the width of the LVZ has a pronounced promotional effect on D_c'' values. The D_c'' values show positive correlation with LVZ width (L_w) for each L_d (Fig. 10a). However, the increase of LVZ depth (L_d) does not always significantly promote the average D_c'' value. This might be related to the competing effects brought by increasing L_d. In one side, larger L_d expands the region of the LVZ and magnifies the D_c''; on the other hand, extending of LVZ depth lowers the rupture speed on the fault plane, which might contribute to the decrease of D_c'' (Supplementary SM2 shows a rupture development movie of a LVZ model). Meanwhile, the calculated D_c'' using the maximum velocity phase in LVZ models (similar to Fig. 9b) show the same increasing pattern with L_w but much larger average values (Fig. 10b). We also conduct simulations with a different velocity reduction value (40 per cent). The effects from velocity reduction values are minor, and variation pattern from LVZ geometry maintains the same at different velocity reduction values. The results with LVZs highlight the importance

of understanding fault zone structures when using the D_c'' method to infer D_c in real cases.

4 DISCUSSION

4.1 Off-fault distance and resolution distance R_c

In Cruz-Atienza *et al.* (2009), a resolution distance R_c is proposed for reasonable D_c'' estimation, which could be estimated by $R_c \approx 0.8 V_S T_c$. V_S is shear wave speed, and T_c refers to the time span of stress breakdown process. In our homogeneous models, $V_S = 3.33$ km s^{-1} and T_c is around 0.5 s, despite the variation in different positions and different models. Substitution into the equation, we get $R_c \approx 1.3$ km for homogeneous models, and smaller values for models with LVZs.

On the other hand R_c could be approximated by the cohesive zone length. The cohesive length varies with depth and time. An average value in the middle depth of the corresponding fault segment is around $1-1.2$ km. In previous sections we analyse the waveforms and D_c'' values within 3 km off-fault distance. The choice of the off-fault range is meant to show the D_c'' values in a broad
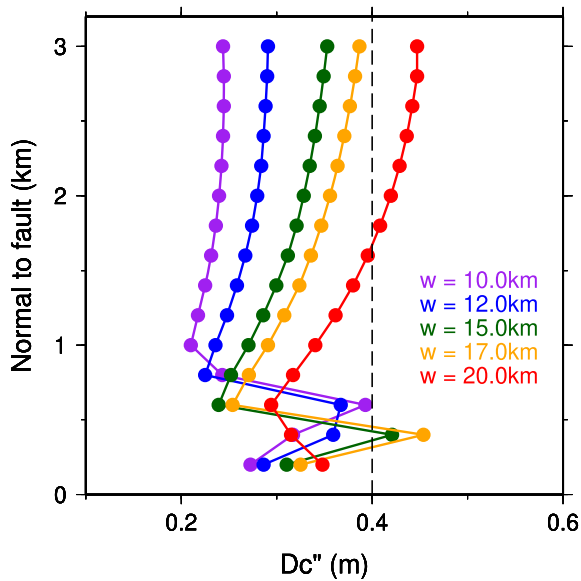
Figure 8. Average D_c'' trend in the fault-normal direction. Each colour corresponds to a seismogenic width. Solid circle on the lines represent an average D_c'' value calculated in a fault-normal distance. The dashed line shows the prescribed $D_c = 0.4$ m.

region based on the current application of D_c'' method, in which the largest off-fault distance is 3 km in Denali earthquake (Fukuyama & Mikumo 2007). A narrower off-fault range would not change the obtained variation trend (Fig. 6a). The mean D_c'' values obtained in the nearest grids still present an increasing trend with seismogenic width (shown as crosses in Fig. 6a). In Fig. 6(b), we show the ground velocity waveforms of nodes with nearest off-fault distance (off-fault distance = 0.2 km) and the corresponding D_c'' values. The increasing tendency of D_c'' with seismogenic width still holds.

4.2 D_c'' and velocity waveforms in fault-normal direction

As ruptures propagate smoothly in the selected area, along strike direction the waveforms show high consistency and D_c'' values are continuous with minor variation in uniform models. In the fault-normal direction, D_c'' presents a piecewise variation pattern as described in Section 3.2 (Figs 7 and 8). The pattern indicates that in the near-field off-fault region, more complex D_c'' values might appear due to the waveform shape change.

The off-fault variation of D_c'' is also calculated in other 3-D spontaneous rupture simulations (Cruz-Atienza *et al.* 2009), in which an increasing trend is shown within around 2 km, different from the features in our results shown in Figs 7 and 8. The near fault complexity in Fig. 7 originates from the waveform shape change as off-fault distance increases, which does not appear in Cruz-Atienza *et al.* (2009). The inconsistency might be related to the difference in profile location. The fault-normal profile in the previous study to show variation in D_c'' values is directly above the nucleation centre, while we show the average value in an area where the rupture propagates tens of kilometres out of the nucleation zone. The

selection in this study intends to avoid the effects from the artificial initial zone and to calculate D_c'' at positions where ruptures grow stably, as shown in Fig. 3. Even though selecting an area in the middle part of the rupture may contain the effects of rupture propagation history, it is a more general choice which diminishes the potential impact from different strategies in rupture initiation.

4.3 Scale dependence of D_c''

In the current application of D_c'' method on real earthquakes, the earthquake magnitudes range from M_w 6.6 to 7.9, with an order of difference in slip amounts (Table 2). As a result, D_c'' increases with slip linearly (Fukuyama & Mikumo 2007; Fukuyama & Suzuki 2016; Kaneko *et al.* 2017). In our models, the average D_c'' values also increase with slip, for example in the models with different seismogenic widths (Fig. 11). As the seismogenic width may affect the moment even with homogeneous parameters (Weng & Yang 2017), such results are well anticipated because D_c'' here is essentially near-field displacement, which is scaled to moment and moment rate (Aki & Richards 2002). However, the prescribed D_c is a constant (i.e. 0.4 m) in all our models, indicating that the scale dependence of D_c'' with slip/moment can not reflect that D_c must be scaled with slip.

Whether dynamic source parameters such as D_c are scale-dependent has been widely investigated in previous studies (Abercrombie & Rice 2005; Tinti *et al.* 2005a, b, 2009; Cocco & Tinti 2008; Viesca & Garagash 2015). The scale-dependent fracture energy from seismological observation might provide indirect constrains on the increasing trend of D_c with earthquake slip (Abercrombie & Rice 2005; Tinti *et al.* 2005b; Cocco & Tinti 2008; Viesca & Garagash 2015), which however still contains uncertainties due to the trade-off between D_c and strength excess. Although recent studies have removed the trade-off using near-field observations and kinematic sources parameters (Weng & Yang 2018; Yao & Yang 2020), it is extremely challenging to distinguish whether D_c is homogeneous or heterogeneous in the condition of heterogeneous stress distribution (Yao & Yang 2020).

4.4 Potential deviation of D_c'' estimation

Utilizing the advantages of numerical simulation, we set numerous of virtual stations on the ground and obtain the average D_c'' using the coherent velocity phase in the stable rupture segment. However, in reality, it is uncommon to have more than one station in the near-fault region (i.e. less than 3 km to the ruptured fault) to capture the coseismic deformation. Therefore, D_c'' is likely inferred from the maximum velocity without coherency correction, as did in previous studies (Fukuyama & Mikumo 2007; Fukuyama & Suzuki 2016; Kaneko *et al.* 2017). As shown in our numerical results, overestimations could be as large as 70 per cent and increase with seismogenic width. If there is a profound LVZ surrounding the ruptured fault, D_c'' obtained at the maximum ground velocity is significantly amplified (Figs 9b and 10b). The overestimation bias at a single location could be as large as twice of the real D_c (Fig. 9b). The near-field complexity requires multiple stations to achieve a better estimation of D_c. Recently, with the increasing deployment of near-fault dense arrays, more near-fault waveform data would become available and provide opportunities to obtain more D_c'' measurements.
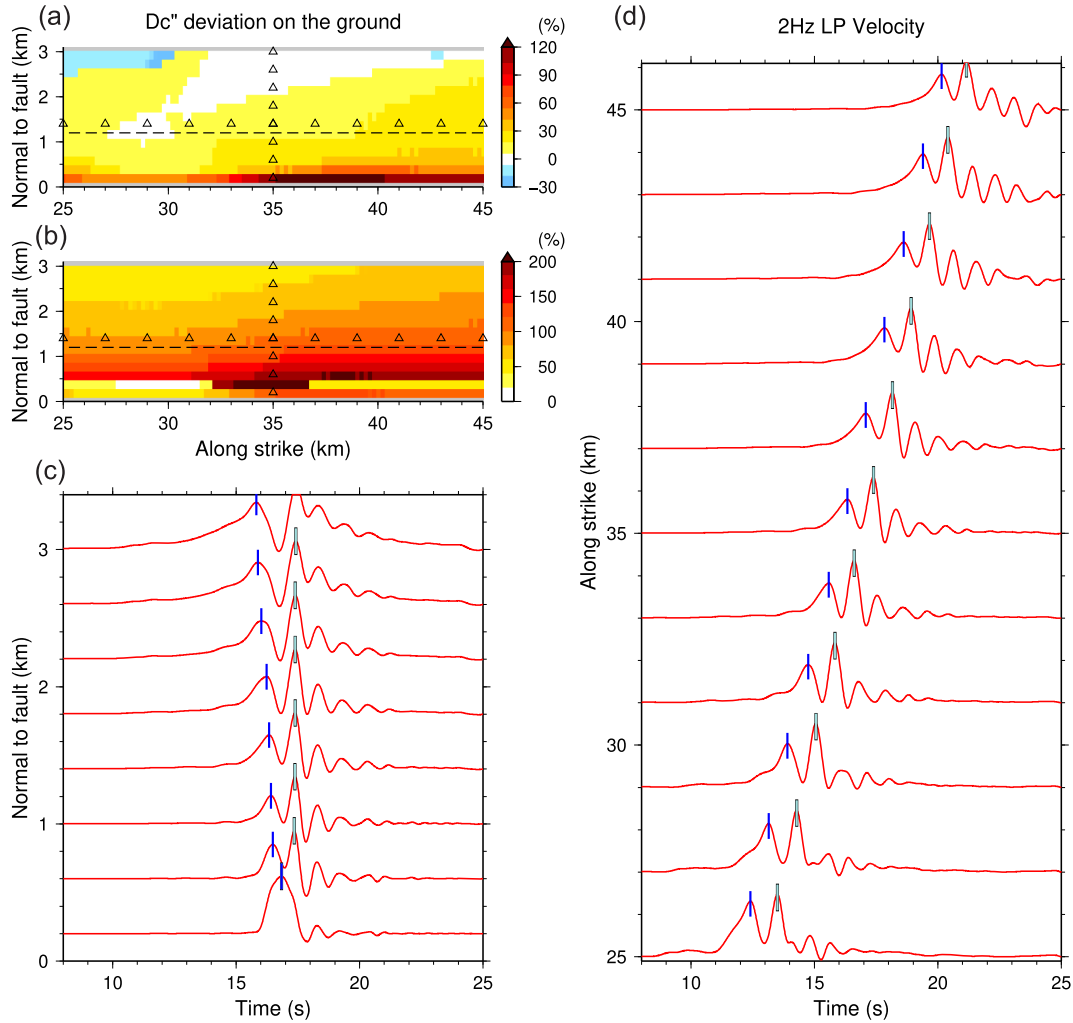
Figure 9. D_c'' deviation and waveform profiles in the LVZ model ($L_w = 2.4$ km, $L_d = 3.0$ km, velocity reduction is 30 per cent). (a) D_c'' deviation degree inferred from the first rupture-related velocity peak after coherency correction. (b) D_c'' deviation degree obtained at the maximum fault-parallel ground velocity time. The dashed line in (a) and (b) marks the one-side range of the LVZ on the ground. Triangles in (a) and (b) show the station locations of profiles in (c) and (d). (c) Fault-parallel ground velocity profile along fault-normal direction (profile location at $x = 35$ km from the initial zone). (d) Fault-parallel ground velocity profile along strike direction (profile location at $y = 1.4$ km off the fault trace). In subfigures (c) and (d), waveforms in red are 2-Hz lowpass filtered fault-parallel velocities. Blue ticks mark the picked time t_p after coherency correcting to determine D_c'' in (a). Light green ticks show the time of the maximum velocity in the waveforms, which leads to a distribution of D_c'' in (b).

Besides seismogenic width and near-fault low velocity zones, there are other potential factors which could play roles in the D_c'' estimation. For example, in this study we use uniform stress distribution in models; as the heterogeneity would lead to heterogeneous slip distribution, it may affect the on-fault D_c' and D_c'' on the ground. Another important factor is the rupture speed. As D_c'' is mainly obtained from strike-slip faults, effects from supershear ruptures need to be considered. One of the four current application cases, Denali earthquake (Table 2), is considered to have supershear rupture speed. From numerical simulations, transient or stable super shear rupture is suggested to be a common phenomenon with the rupture reaches the free surface (Kaneko & Lapusta 2010; Xu *et al.* 2015). In Fig. S4, we show the results from different S ratios ($S = \frac{\tau_s - \tau_0}{\tau_0 - \tau_d}$, Andrews 1976) as the S ratio impacts the rupture speed and occurrence of supershear rupture (Dunham 2007). In a bounded fault, the S ratio would also affect rupture transition from breakaway to self-arresting

(Weng & Yang 2017). Thus, the effects of the S ratio and rupture speed might be significant and thus may demand additional work to investigate.

5 CONCLUSION

We conduct numerical simulations of 3-D spontaneous ruptures to investigate the estimation results of D_c using D_c'' values, regarding the effects of seismogenic width and low-velocity zones. We pick the first rupture-related peak from lowpass filtered ground velocity and obtain D_c'' from the ground displacements within a selected area where the stable rupture is established. With a constant prescribed D_c on the homogeneous fault, the obtained D_c'' from the ground surface shows positive correlation with seismogenic width, as the amplitude of ground velocity increases with the width. With
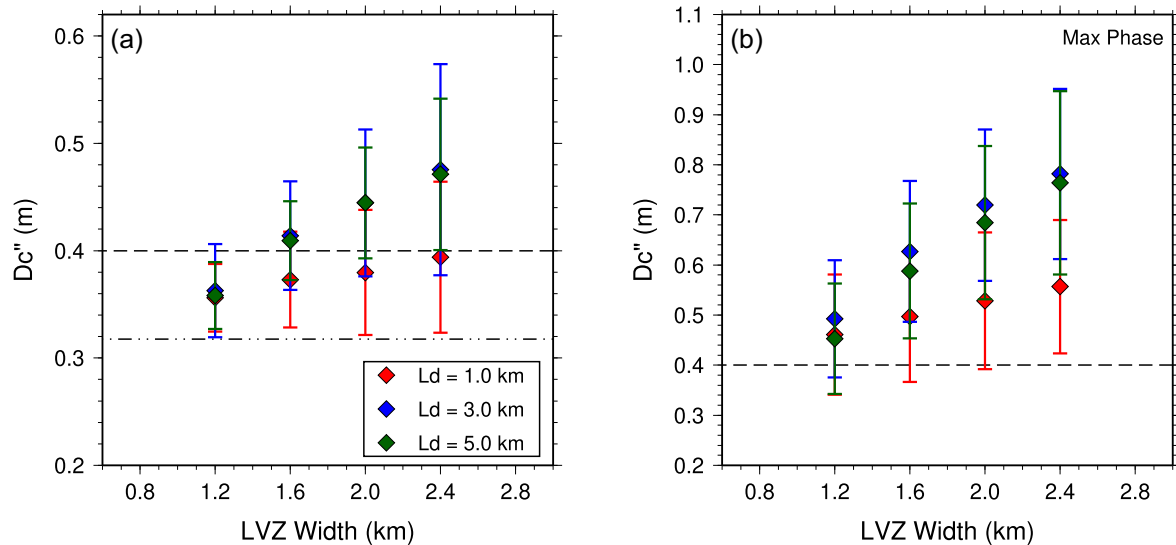
Figure 10. Average D_c'' values versus L_w. D_c'' values in (a) are obtained using the first rupture-related velocity peak after coherency correcting (similar to Fig. 9a). D_c'' values in (b) are obtained at the maximum fault-parallel ground velocity time (similar to Fig. 9b). Red, blue and green diamonds represent models with $L_d = 1.0$, 3.0 and 5.0 km, respectively. The dashed lines mark the prescribed constant $D_c = 0.4$ m. The dashed−dotted line shows the average D_c'' value in the uniform model without the LVZ.
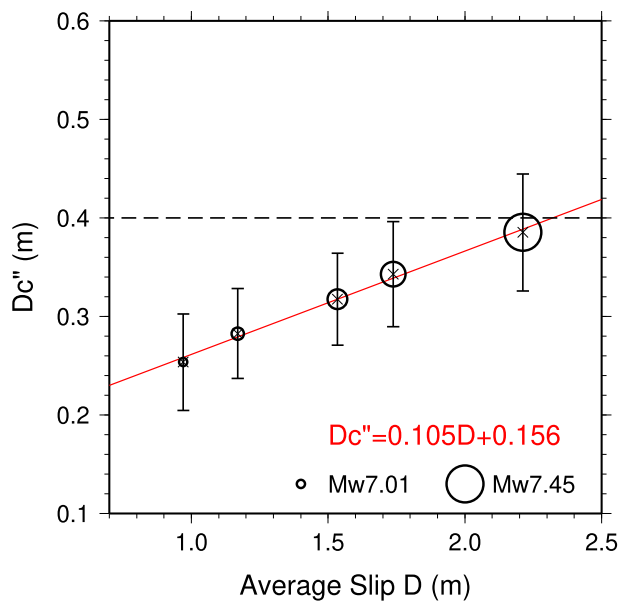
Figure 11. Average D_c'' values versus slip in uniform models. Radii of the circles correspond to the magnitudes of the scenario earthquakes. The red line shows the least square fitting of the data points, with the expression equation shown in red. The dashed line marks the prescribed constant $D_c = 0.4$ m.

the existence of the LVZ, the ground velocity is amplified and complicated with multiwiggles, and the corresponding D_c'' is magnified. The complex wavefields introduced by the LVZ might lead to large overestimation when using D_c'' at the maximum velocity time to estimate D_c. The width of the LVZ plays a more prominent effect on enlarging D_c'' compared to LVZ depth. The numerical results indicate that the obtained scale dependence based on D_c'' might be affected by the effects of fault geometry and material properties,

such as seismogenic zone width and low-velocity zones. Overestimation should be considered when using D_c'' from limited near-fault stations to infer D_c on real faults.

REFERENCES

Aagaard, B.T., Knepley, M.G. & Williams, C.A., 2013. A domain decomposition approach to implementing fault slip in finite-element models of quasi-static and dynamic crustal deformation, *J. geophys. Res.,* **118,** 3059–3079.

Abercrombie, R.E. & Rice, J.R., 2005. Can observations of earthquake scaling constrain slip weakening?, *Geophys. J. Int.,* **162,** 406–424.

Aki, K. & Richards, P.G., 2002. *Quantitative Seismology,* 2nd edn, University Science Books.

Andrews, D.J., 1976. Rupture velocity of plane strain shear cracks, *J. geophys. Res.,* **81,** 5679–5687.

Ben-Zion, Y. & Aki, K., 1990. Seismic radiation from an SH line source in a laterally, *Bull. seism. Soc. Am,* **80,** 971–994.

Ben-Zion, Y. & Sammis, C.G., 2003. Characterization of fault zones, *Pure appl. Geophys.,* **160,** 677–715.

Bizzarri, A., 2010. How to promote earthquake ruptures: different nucleation strategies in a dynamic model with slip-weakening friction, *Bull. seism. Soc. Am.,* **100,** 923–940.

Bizzarri, A., Dunham, E.M. & Spudich, P., 2010. Coherence of Mach fronts during heterogeneous supershear earthquake rupture propagation: simulations and comparison with observations, *J. geophys. Res.,* **115,** 1–22.

Bouchon, M., 1997. The state of stress on some faults of the San Andreas System as inferred from near-field strong motion data, *J. geophys. Res.,* **102,** 11 731–11 744.

Cocco, M. & Tinti, E., 2008. Scale dependence in the dynamics of earthquake propagation: evidence from seismological and geological observations, *Earth planet. Sci. Lett.,* **273,** 123–131.

Courant, R., Friedrichs, K. & Lewy, H., 1928. Über die partiellen ifferenzengleichungen der mathematischen Physik, *Math. Ann.,* **100,** 32–74.

Cruz-Atienza, V.M., Olsen, K.B. & Dalguer, L.A., 2009. Estimation of the breakdown slip from strong-motion seismograms: insights from numerical experiments, *Bull. seism. Soc. Am.,* **99,** 3454–3469.

Dalguer, L.A., Irikura, K., Zhang, W. & Riera, J.D., 2002. Distribution of dynamic and static stress changes during 2000 Tottori (Japan) earthquake: brief interpretation of the earthquake sequences; foreshocks, mainshock and aftershocks, *Geophys. Res. Lett.,* **29,** 5-1-5-4.

Day, S.M., 1982. Three-dimensional finite difference simulation of fault dynamics: rectangular faults with fixed rupture velocity, *Bull. seism. Soc. Am.,* **72,** 705–727.

Day, S.M., Dalguer, L.A., Lapusta, N. & Liu, Y., 2005. Comparison of finite difference and boundary integral solutions to three-dimensional spontaneous rupture, *J. geophys. Res.,* **110,** 1–23.

Di Toro, G., Han, R., Hirose, T., De Paola, N., Nielsen, S., Mizoguchi, K., Ferri, F., Cocco, M. & Shimamoto, T., 2011. Fault lubrication during earthquakes, *Nature,* **471,** 494–498.

Dunham, E.M., 2007. Conditions governing the occurrence of supershear ruptures under slip-weakening friction, *J. geophys. Res.,* **112,** 1–24.

Dunham, E.M. & Archuleta, R.J., 2004. Evidence for a Supershear transient during the 2002 Denali fault earthquake **94,** 256–268.

Fukuyama, E., 2003. Estimation of the critical slip-weakening distance: theoretical background, *Bull. seism. Soc. Am.,* **93,** 1835–1840.

Fukuyama, E. & Mikumo, T., 2007. Slip-weakening distance estimated at near-fault stations, *Geophys. Res. Lett.,* **34,** 2–6.

Fukuyama, E. & Suzuki, W., 2016. Near-fault deformation and Dc$''$ during the 2016 Mw7.1 Kumamoto earthquake, *Earth, Planets Space.*, **68,** 6–11.

Galis, M., Pelties, C., Kristek, J., Moczo, P., Ampuero, J.-P. & Mai, P.M., 2015. On the initiation of sustained slip-weakening ruptures by localized stresses, *Geophys. J. Int.,* **200,** 888–907.

Goldsby, D.L. & Tullis, T.E., 2011. Flash heating leads to low frictional strength of crustal rocks at earthquake slip rates, *Science,* **334,** 216–218.

Goto, H. & Sawada, S., 2010. Trade-offs among dynamic parameters inferred from results of dynamic source inversion, *Bull. seism. Soc. Am.,* **100,** 910–922.

Guatteri, M., 2000. What can strong-motion data tell us about slip-weakening fault-friction laws?, *Bull. seism. Soc. Am.,* **90,** 98–116.

Houston, H., 2015. Low friction and fault weakening revealed by rising sensitivity of tremor to tidal stress, *Nat. Geosci.,* **8,** 409–415.

Huang, Y. & Ampuero, J.P., 2011. Pulse-like ruptures induced by low-velocity fault zones, *J. geophys. Res.,* **116,** 1–13.

Ida, Y., 1972. Cohesive force across the tip of a longitudinal-shear crack and Griffith's specific surface energy, *J. geophys. Res.,* **77,** 3796–3805.

Ide, S. & Takeo, M., 1997. Determination of constitutive relations of fault slip based on seismic wave analysis, *J. geophys. Res.,* **102,** 27 379–27 391.

Kaneko, Y., Fukuyama, E. & Hamling, I.J., 2017. Slip-weakening distance and energy budget inferred from near-fault ground deformation during the 2016 Mw7.8 Kaikōura earthquake, *Geophys. Res. Lett.,* **44,** 4765–4773.

Kaneko, Y. & Lapusta, N., 2010. Tectonophysics Supershear transition due to a free surface in 3-D simulations of spontaneous dynamic rupture on vertical strike-slip faults, *Tectonophysics,* **493,** 272–284.

Kurzon, I., Vernon, F.L., Ben-Zion, Y. & Atkinson, G., 2014. Ground motion prediction equations in the San Jacinto fault zone: significant effects of rupture directivity and fault zone amplification, *Pure appl. Geophys.,* **171,** 3045–3081.

Ma, S., Custódio, S., Archuleta, R.J. & Liu, P., 2008. Dynamic modeling of the 2004 Mw 6.0 Parkfield, California, earthquake, *J. geophys. Res.,* **113,** 1–16.

Mikumo, T., Olsen, K.B., Fukuyama, E. & Yagi, Y., 2003. Stress-breakdown time and slip-weakening distance inferred from slip-velocity functions on earthquake faults, *Bull. seism. Soc. Am.,* **93,** 264–282.

Nielsen, S.B. & Olsen, K.B., 2000. Constraints on stress and friction from dynamic rupture models of the 1994 Northridge, California, earthquake, *Pure appl. Geophys.,* **157,** 2029–2046.

Olsen, K.B., Madariaga, R. & Archuleta, R.J., 1997. Three-dimensional dynamic simulation of the 1992 Landers earthquake, *Science,* **278,** 834–838.

Palmer, A.C. & Rice, J.R., 1973. The growth of slip surfaces in the progressive failure of over-consolidated clay, *Proc. R. Soc. Lond., A.,* **332,** 527–548.

Reches, Z. & Lockner, D.A., 2010. Fault weakening and earthquake instability by powder lubrication, *Nature,* **467,** 452–455.

Spudich, P., 2005. The effect of bandwidth limitations on the inference of earthquake slip-weakening distance from seismograms, *Bull. seism. Soc. Am.,* **94,** 2028–2036.

Tinti, E., Cocco, M., Fukuyama, E. & Piatanesi, A., 2009. Dependence of slip weakening distance (Dc) on final slip during dynamic rupture of earthquakes, *Geophys. J. Int.,* **177,** 1205–1220.

Tinti, E., Fukuyama, E., Piatanesi, A. & Cocco, M., 2005a. A kinematic source-time function compatible with earthquake dynamics, *Bull. seism. Soc. Am.,* **95,** 1211–1223.

Tinti, E., Spudich, P. & Cocco, M., 2005b. Earthquake fracture energy inferred from kinematic rupture models on extended faults, *J. geophys. Res.,* **110,** B12303.

Viesca, R.C. & Garagash, D.I., 2015. Ubiquitous weakening of faults due to thermal pressurization, *Nat. Geosci.,* **8,** 875–879.

Weng, H. & Yang, H., 2017. Seismogenic width controls aspect ratios of earthquake ruptures, *Geophys. Res. Lett.,* **44,** 2725–2732.

Weng, H. & Yang, H., 2018. Constraining frictional properties on fault by dynamic rupture simulations and near-field observations, *J. geophys. Res.,* **123,** 6658–6670.

Weng, H., Yang, H., Zhang, Z. & Chen, X., 2016. Earthquake rupture extents and coseismic slips promoted by damaged fault zones, *J. geophys. Res.,* **121,** 4446–4457.

Wibberley, C.A.J. & Shimamoto, T., 2005. Earthquake slip weakening and asperities explained by thermal pressurization, *Nature,* **436,** 689–692.

Wu, C., Peng, Z. & Ben-zion, Y., 2009. Non-linearity and temporal changes of fault zone site response associated with strong ground motion, *Geophys. J. Int.,* **176,** 265–278.

Xu, J., Zhang, H. & Chen, X., 2015. Rupture phase diagrams for a planar fault in 3-D full-space and half-space, *Geophys. J. Int.,* **202,** 2194–2206.

Yang, H., 2015. Recent advances in imaging crustal fault zones: a review, *Earthq. Sci.,* **28,** 151–162.

Yang, H., Duan, Y., Song, J., Jiang, X., Tian, X., Yang, W., Wang, W. & Yang, J., 2020. Fine Structure of the Chenghai Fault Zone, Yunnan, China, Constrained From Teleseismic Travel Time and Ambient Noise Tomography, *J. geophys. Res.,* **125**(7), e2020JB019565.

Yang, H., Liu, Y. & Lin, J., 2013. Geometrical effects of a subducted seamount on stopping megathrust ruptures, *Geophys. Res. Lett.,* **40,** 2011–2016.

Yang, H., Li, Z., Peng, Z., Ben-Zion, Y. & Vernon, F., 2014. Low-velocity zones along the San Jacinto Fault, Southern California, from body waves recorded in dense linear arrays, *J. geophys. Res.,* **119,** 8976–8990.

Yang, H. & Yao, S., 2019. In-situ frictional properties on seismogenic faults inferred from near-field observations and numerical simulations, in *Proceedings of the EGU General Assembly 2019*. p. 12466.

Yang, H., Yao, S., He, B. & Newman, A. V., 2019. Earthquake rupture dependence on hypocentral location along the Nicoya Peninsula subduction megathrust, *Earth planet. Sci. Lett.,* **520,** 10–17.

Yang, H. & Zhu, L., 2010. Shallow low-velocity zone of the San Jacinto fault from local earthquake waveform modelling, *Geophys. J. Int.,* **183,** 421–432.

Yang, H., Zhu, L. & Cochran, E.S., 2011. Seismic structures of the Calico fault zone inferred from local earthquake travel time modelling, *Geophys. J. Int.,* **186,** 760–770.

Yao, S. & Yang, H., 2020. Rupture dynamics of the 2012 Nicoya Mw7.6 earthquake: evidence for low strength on the megathrust, *Geophys. Res. Lett.,* **47**(13), e2020GL087508,.

SUPPORTING INFORMATION

Supplementary data are available at *GJI* online.

Figure S1. Comparison of simulated rupture results of different grid sizes. (a) Rupture isochrones contours on the fault plane in a homogeneous model with $w = 15$ km. The red dashed lines, black lines and blue dotted lines are rupture isochrones of models with grid $\Delta x = 150$ m, $\Delta x = 200$ m and $\Delta x = 250$ m, respectively. Triangles represent the virtual station locations to show the slip rate waveforms. Panels (b)−(d) are comparison of slip rate waveforms at different locations, which are declared on the top of each subfigure. A 2 Hz lowpass filter is applied to the slip rate waveforms.

Figure S2. Comparison of simulated ground waveforms of different grid sizes. Panels (a)−(c) show the raw data of fault-parallel velocities at different locations. Panels (d)−(e) show the 2 Hz lowpass filtered waveform data. The grid location is declared on top of each column. Red, black and blue curves correspond to the grid sizes of $\Delta x = 150$ m, $\Delta x = 200$ m and $\Delta x = 250$ m, respectively. The model shown in this figure is uniform with $w = 15$ km.

Figure S3. D_c' deviation on the fault plane. (a) D_c' deviation degree of the raw data. (b) D_c' deviation degree inferred from 2 Hz lowpass filtered slip rate. Triangles in (a) and (b) shows the grid locations of the waveforms in (c). (c) Slip rate waveforms and shear stress change. Red curves are 2 Hz lowpass filtered slip rate waveforms, beneath which black curves show the raw data. Blue curves show the shear stress. Dashed lines mark the peak slip rate time. The waveform profile is located at the middle depth $z = -7.6$ km, shown as triangles in (a) and (b). The model shown in this figure is uniform with $w = 15$ km.

Figure S4. Average D_c'' values with different S ratios. (a) Average D_c'' versus seismogenic width. (b) Average D_c'' versus average rupture speed. The average values are calculated in the 20 km (along-strike) $\times$ 3 km (normal-to-fault) area as shown in Fig. 5. Red, black, blue and green symbols correspond to S ratio = 1.1, 1.2, 1.3 and 1.4, respectively. S ratio = 1.2 is set for all of other models in this study. Transient supershear occurs in the selected area for the model with S ratio = 1.2, $w = 24$ km. For models with S ratio = 1.4, the rupture turns into self-arresting in $w = 20$ km, which does not break the whole fault.

SM1. Animation of the fault-parallel ground velocity on the ground surface and the slip rate on the fault plane. This is output from a uniform model with seismogenic width $w = 15$ km.

SM2. Animation of the fault-parallel ground velocity on the ground surface and the slip 48 rate on the fault plane. This is output from a model with the low-velocity zone ($L_w = 2.4$ km, $L_d = 3.0$ km, velocity reduction is 30%).

Please note: Oxford University Press is not responsible for the content or functionality of any supporting materials supplied by the authors. Any queries (other than missing material) should be directed to the corresponding author for the paper.